Influence of Sn addition on microstructure and corrosion resistance of AS21 magnesium alloy

Huseyin ZENGIN[1], Yunus TUREN[1], Hayrettin AHLATCI[1], Yavuz SUN[1], Abdullah Cahit KARAOĞLANLI[2]

1. Department of Metallurgical and Materials Engineering, Karabuk University, Turkey;
2. Department of Metallurgical and Materials Engineering, Bartın University, Turkey

Abstract: This study aims to investigate the influence of Sn addition on microstructure and corrosion properties of AS21 magnesium alloys. The AS21 alloys with 0, 0.5, 1 and 2 wt.% Sn additions were produced by low pressure die casting method. Microstructure characterizations were performed by optical and scanning electron microscopy. Corrosion properties of the alloys were examined by immersion and electrochemical corrosion tests in 3.5% NaCl solution. The microscopic results showed that AS21 alloy consisted of α-Mg, isolated β-$Mg_{17}Al_{12}$ and Chinese script type Mg_2Si intermetallic phases. With increasing amount of Sn, the distribution of Mg_2Si phase became more discrete and denser. After 2 wt.% Sn addition, a Sn-rich network structure formed throughout the microstructure and islands of Chinese script shape were made of shorter rods of Mg_2Si phase. The constant immersion corrosion tests revealed that increasing Sn addition led to a continual decrease in the degradation of AS21 alloys, in which the corrosion rate of AS21 alloy was decreased by approximately 65% with 2 wt.% Sn addition. The electrochemical corrosion tests also showed that the corrosion resistance of AS21 alloy was gradually improved with increasing Sn content.
Key words: AS21; magnesium alloy; Sn addition; microstructure; corrosion

1 Introduction

In recent years, magnesium alloys have attracted more attention to be used as structural metal in automotive and aerospace industries due to their uniquely high specific strength [1]. However, magnesium alloys suffer from primarily low corrosion, wear and creep resistances which extremely limit their widespread applications [1,2]. It is well known that, AZ91 alloy is the most commercially-used magnesium alloy since it provides optimum combination of strength and ductility at room temperature [2]. However, at elevated temperatures, the mechanical properties of AZ91 alloy easily deteriorate because of the presence of low thermally-stable β-$Mg_{17}Al_{12}$ phase [3,4]. Therefore, Mg−Al−Si alloys (AS series) containing few β-$Mg_{17}Al_{12}$ phase and large amount of Mg_2Si phase were developed in order to obtain better mechanical properties at elevated temperatures than AZ series magnesium alloys [3]. The improved mechanical properties at elevated temperatures are majorly due to the formation of Mg_2Si intermetallic phase with a high melting temperature, hardness and elastic modulus and low thermal expansion coefficient and density [1,3]. BLUM et al [4] compared the creep resistance of AS21, AS41, AZ91, AM60 and AE42 alloys and showed that AS series alloys exhibited the best creep resistance at low stresses. ZHANG [5] showed that rod-shaped Mg_2Si precipitates hardened AS21 alloy and breakage of these precipitates resulted in a work softening during tertiary creep. TANG et al [6] reported that the morphology of Mg_2Si phase changed from Chinese script type to fibre shape by the addition of Al−10%Sr master alloy.

Although numerous studies have been conducted on the creep properties of AS series magnesium alloys, there are limited studies that investigate the effect of different alloying elements on corrosion resistance of AS series magnesium alloys [7−9]. SENF et al [7] compared the corrosion resistance of AS41, AZ91, AM60 and AE42 alloys under salt spray conditions and reported an order of corrosion resistance of the studied alloys as AE42> AZ91>AM60>AS41. A recent study [9] investigated the corrosion behavior of various Mg−Al−Si alloys (AS11, AS21, AS41, AS61 and AS91) and reported that AS21 alloy exhibited the best corrosion behavior and

increasing Al content above 2 wt.% resulted in a continual degradation of corrosion resistance due to the creation of more galvanic sites caused by β-$Mg_{17}Al_{12}$ phase.

In recent years, Sn-containing magnesium alloys have come to the forefront due to the promising effect of Sn. Numerous studies have agreed that Sn addition results in an improvement on the mechanical properties of magnesium alloys by primarily forming fine Mg_2Sn precipitates in the microstructure [10−12]. Additionally, it was reported that Sn can significantly improve the age hardening response in AZ91 alloy and also change the precipitation behaviour of β-$Mg_{17}Al_{12}$ phase by suppressing discontinuous precipitation and accelerating continuous precipitation [13]. A more recent study by SEDIGHI et al [14] investigated the effect of Sn on solidification behavior of AZ91 alloy and they reported that 0.5 wt.% Sn addition exhibited the best solidification behavior such as high nucleation temperature and low recalescence undercooling. Furthermore, several studies investigated the effect of Sn on corrosion properties of magnesium alloys [12,15,16]. WANG et al [12] showed that 0.5 wt.% Sn addition improved the corrosion resistance of Mg−7Al−1Ca alloy due to the refinement of grain and intermetallic phases and the disappearance of $(Mg,Al)_2Ca$ phase. PARK et al [15] investigated the effect of various Sn additions (0, 1, 5 and 9 wt.% Sn) on the corrosion behavior of Mg−5Al−1Zn alloy and reported that 5 wt.% Sn addition significantly improved the corrosion resistance. SONG [16] showed that 2 wt.% Sn addition to AM70 resulted in less amount of localized galvanic corrosion although a higher amount of overall metal loss was observed.

Since most of the studies have been focused on the corrosion behavior of Sn-containing AZ and AM series magnesium alloys, there is less study investigating the effect of low amount of Sn additions on corrosion behavior of AS series alloys. Therefore, this study aims to improve and understand the effect of Sn additions up to 2 wt.% on corrosion behavior of AS21 magnesium alloys.

2 Experimental

The Mg−2wt.%Al−1wt.%Si alloys with various Sn additions (0, 0.5, 1 and 2 wt.%) were produced by low pressure die casting method. The compositions of the produced alloys were determined by wave-length dispersion X-ray fluorescence (XRF) and listed in Table 1. The alloys were prepared by melting pure Mg (99.9%), Al (99.9%), Sn (99.9%) and Al−30%Si master alloys in a steel crucible placed in an air tight electric resistance furnace under controlled argon (Ar) gas atmosphere. After holding the melt at 750 °C for 45 min, a stirring for

15 min was applied in order to dissolve alloying elements and provide compositional homogeneity. At the melt temperature of 720 °C, an Ar gas pressure of 2×10^5 Pa was applied into the crucible and the preheated (at 250 °C) steel mould was filled through the steel pipe with a filling time of 2 s. The dimension of the cast billet was d34 mm×190 mm.

Table 1 Chemical compositions of AS21 alloys (wt.%)

Alloy	Al	Si	Sn	Mn	Mg
AS21	2.12	1.11	−	0.21	Bal.
AS21−0.5Sn	2.22	1.09	0.57	0.23	Bal.
AS21−1Sn	2.24	1.03	1.16	0.18	Bal.
AS21−2Sn	2.05	0.98	2.01	0.25	Bal.

Microstructural characterizations were carried out by optical microscopy (OM) and scanning electron microscopy (SEM). Before the microstructure analysis, all the samples were mechanically ground with 240, 400, 600, 800, 1000, 1200 and 2000 grit emery papers followed by polishing with 6 μm and 1 μm diamond paste. The polished samples were etched with 3% HNO_3.

The cylindrical specimens for immersion corrosion tests having d8 mm×20 mm dimensions were cut from the half radius of the alloys and subsequently ground and polished followed by ultrasonic cleaning in alcohol for 10 min. Then, the specimens were weighed before the test with an accuracy of the weighing balance of 0.1 mg and immersed in 3.5 wt.% NaCl solution at room temperature for 72 h. The exposed area of the specimens in the immersion corrosion tests was 603 mm^2. After the immersion test, the formed corrosion products on the surface were removed by a solution of 180 g/L chromic acid followed by cleaning with alcohol according to ASTM−G31−72 standard [17]. The corrosion rate of the samples after immersion test, P_w, was also calculated according to the following equation [17]:

$$P_w=K·W/(A·T·D) \tag{1}$$

where $K(=8.76\times10^4)$ is a constant in mm/a, W is the mass loss in g, A is the exposed surface area in cm^2, T is the immersion time in h and D is the density of tested samples in g/cm^3. The experimental densities of samples were measured with digital density meter according to the Archimedes' principle and the average density values obtained from at least three readings for each sample are given in Table 2. The corrosion products after 6 h immersion were investigated by SEM and the corroded surfaces of the alloys immersed for 72 h were investigated after removal of corrosion products by OM and SEM to determine the corrosion mechanisms.

The potentiodynamic polarization corrosion tests were also performed in 3.5 wt.% NaCl solution by a

Table 2 Densities of alloys

Alloy	Theoretical density/ $(\text{g}\cdot\text{cm}^{-3})$	Experimental density/ $(\text{g}\cdot\text{cm}^{-3})$
AS21	1.763	1.759
AS21−0.5Sn	1.791	1.785
AS21−1Sn	1.819	1.810
AS21−2Sn	1.875	1.871

Gamry model PC4/300 mA potentiostat/galvanostat with DC105 corrosion analysis at a scan rate of 1 mV/s, starting from −0.25 to +0.25 V. The corrosion potentials (φ_{corr}) and the corrosion current densities (J_{corr}) were determined by applying Tafel extrapolation method on the obtained polarization curves. A standard three-electrode cell was used consisting of a reference electrode (saturated calomel electrode), a counter electrode (graphite rod, d6 mm), and a working electrode (the sample). The corrosion rate of the samples after potentiodynamic polarization tests, P_i, was calculated according to ASTM−G102−89 standard [18] by the following equation:

$$P_i = \lambda \cdot J_{corr} \cdot E/D \tag{2}$$

where $\lambda (=3.27 \times 10^{-3})$ is the metric conversion factor in $(\text{mm}\cdot\text{g})/(\mu\text{A}\cdot\text{cm}\cdot\text{a})$, J_{corr} is the corrosion current density in $\mu\text{A}/\text{cm}^2$, E is the equivalent mass.

In the EIS tests, the frequency range was set from 10 kHz to 0.1 Hz and the voltage amplitude was set to be 10 mV. Both electrochemical tests were repeated at least three times to supply reproducibility. Both the immersion and electrochemical corrosion tests were conducted in a temperature-controlled laboratory (at 20 °C).

3 Results and discussion

3.1 Microstructure

Figure 1 shows the optical micrographs of AS21 alloys with 0, 0.5, 1 and 2 wt.% Sn additions. The microstructure of the alloys consisted of primarily α-Mg solid solution (white matrix) and secondary phases (dark regions) with different morphologies. Two distinct morphologies of the secondary phases were observed in the microstructures: Chinese script type and divorced particles. Previous studies [4,9,19] reported that AS21 alloys consistently contained large amount of Chinese script type Mg_2Si phase and a few amounts of divorced or partially-divorced β-$Mg_{17}Al_{12}$ phase. Similarly, large amount of wide Chinese script type Mg_2Si phase and few isolated β-$Mg_{17}Al_{12}$ phase islands were observed in AS21 alloy, as seen in Fig. 1(a). With increasing Sn content, Chinese script type Mg_2Si intermetallic phase appeared to be refined and the distribution of Chinese script Mg_2Si became more discrete but its shape changed into short and bold closely-spaced rods of Mg_2Si intermetallics. It is also clear that Sn addition gave rise to a formation of gray regions in the vicinity of second phases and the
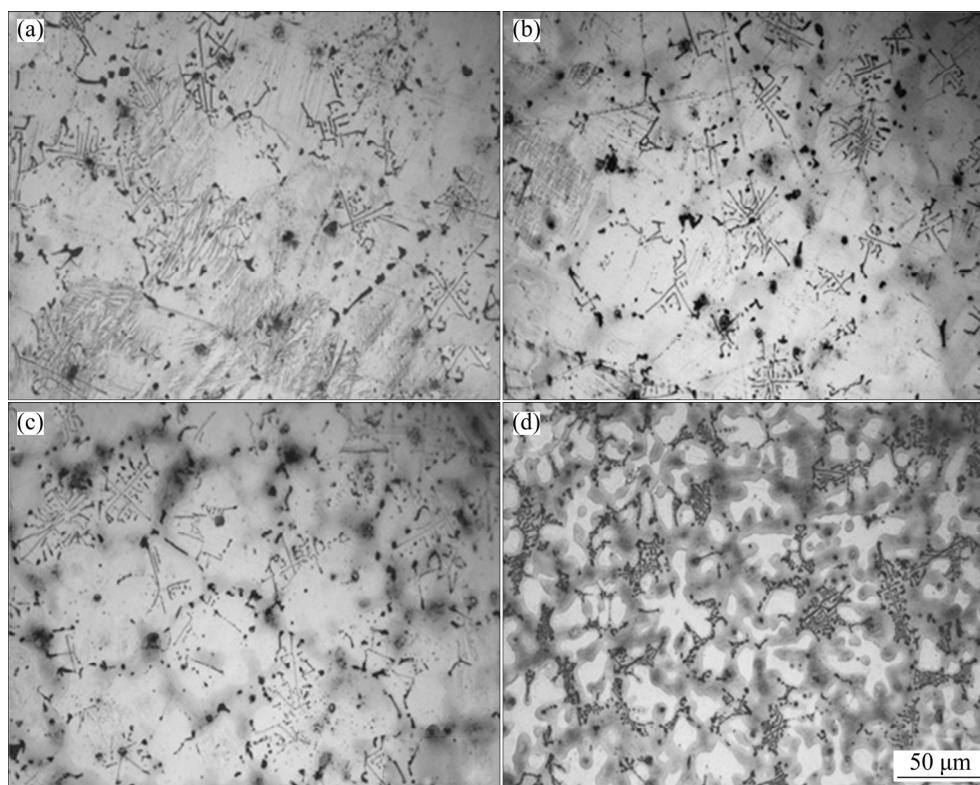

Fig. 1 Optical micrographs of AS21 (a), AS21−0.5Sn (b), AS21−1Sn (c) and AS21−2Sn (d) alloys

fraction of these regions continually increased as the Sn content was increased to 2 wt.%. AS21−2Sn alloy had the finest Chinese script type Mg_2Si, indicating that Sn addition resulted in a suppression of the growth of Chinese script shape Mg_2Si phases.

Figure 2 shows SEM micrographs of AS21 and AS21−2Sn alloys with corresponding line EDS results. By comparing the line EDS results of the phases, Mg and Si elements were enriched in Chinese script type Mg_2Si phase in AS21 alloy but after 2 wt.% Sn addition, Sn peaks were observed within Chinese script type Mg_2Si phase. As shown in Figs. 2(e, f), Sn compositions in Chinese script type Mg_2Si phase were found to be around 3.5−4.5 wt.%. It was reported that Sn was mainly found

in α-Mg matrix as solute elements and as $Mg_2(Sn,Si)$ [20], confirming the similar findings of this study. It should also be noted that primarily Sn and Al enrichment in the gray region occurred in AS21−2Sn alloy, as shown in Fig. 2(d). Since Sn has a high maximum solubility in Mg (14.85 wt.%) [21], Mg−Sn binary intermetallic phases were not expected to be precipitated by an addition of up to 2 wt.% Sn. Accordingly, no Mg_2Sn phase was encountered during microstructure characterizations and all Sn elements were preferentially located within Chinese script Mg_2Si phase and gray regions due to segregation during solidification [22]. These Sn-rich regions generated a continuous network structure throughout the microstructure in AS21−2Sn alloy.
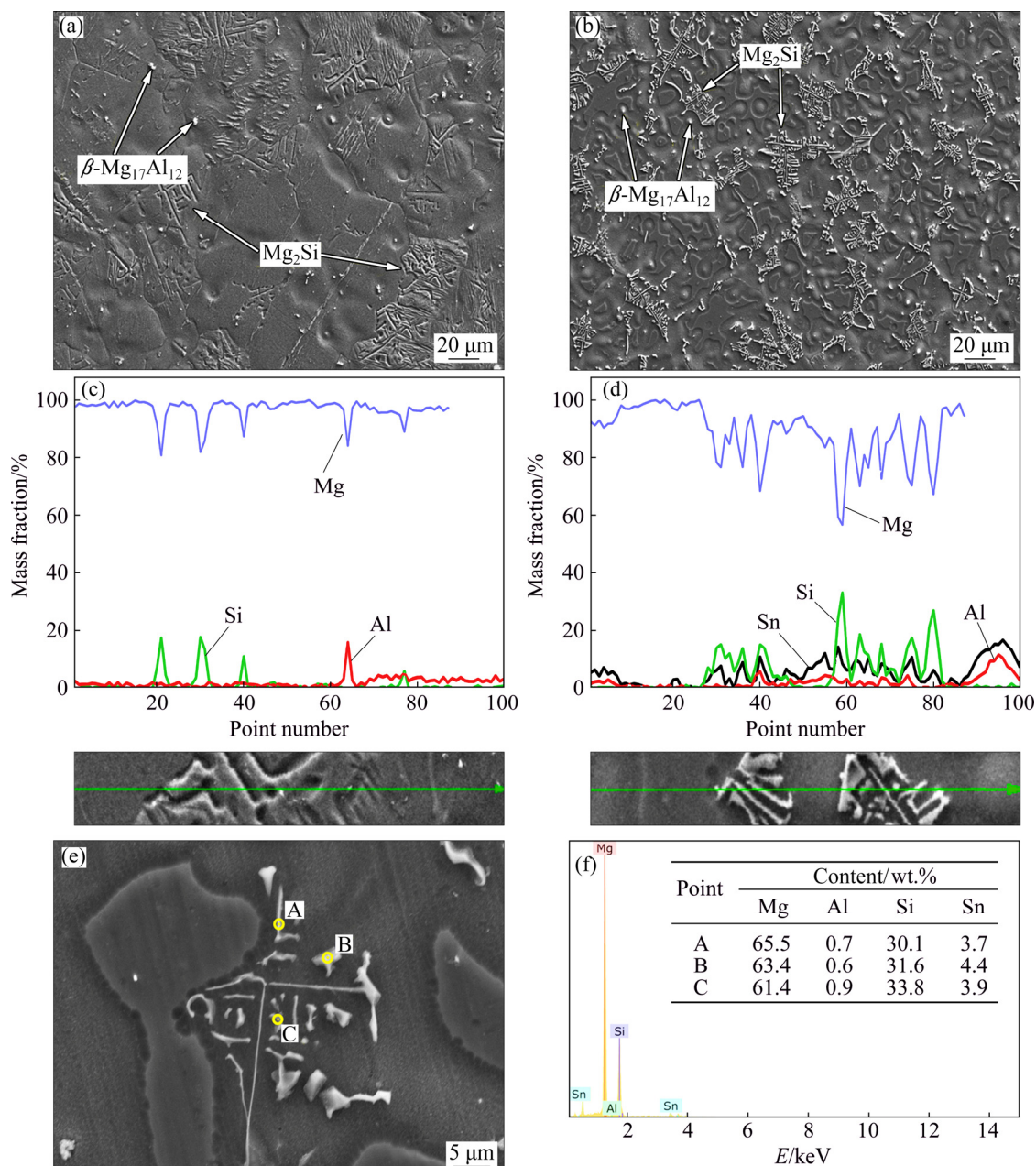

Fig. 2 SEM micrographs (a, b, e), line EDS results of phases (c, d) in AS21 (a, c) and AS21−Sn (b, d, e) and point EDS results (f) of points in (e)

3.2 Corrosion

Figure 3 illustrates the mass loss per unit area and time as a function of Sn content in AS21 alloys exposed in 3.5% NaCl solution for 72 h. Besides, corresponding macroscopic images taken after the immersion test were also shown. The calculated corrosion rates (P_w) according to Eq. (1) are given in Table 3. It is evident that the mass loss rate gradually decreased with increasing Sn content. Macroscopic images of the alloys revealed that AS21 alloy suffered from severe corrosion throughout the surface. However, after 0.2 wt.% Sn addition, a partial severe corrosion on the surface took place and the degree of corrosion showed a continual decrease with increasing Sn content up to 2 wt.%.

Figure 4 shows the SEM micrographs taken after the removal of corrosion products of the alloys immersed
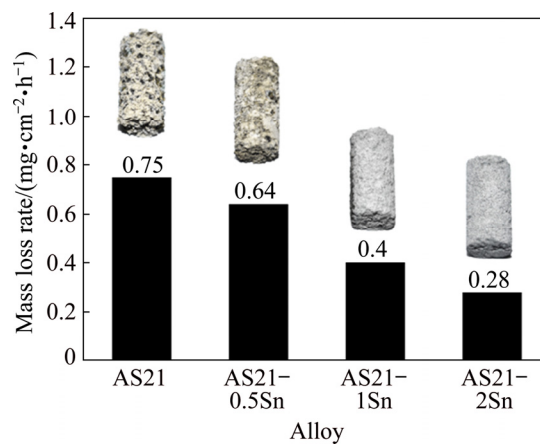

Fig. 3 Average corrosion rate of AS21 alloys as function of Sn content with corresponding macroscopic images of corrosion specimens after immersion in 3.5% NaCl for 72 h
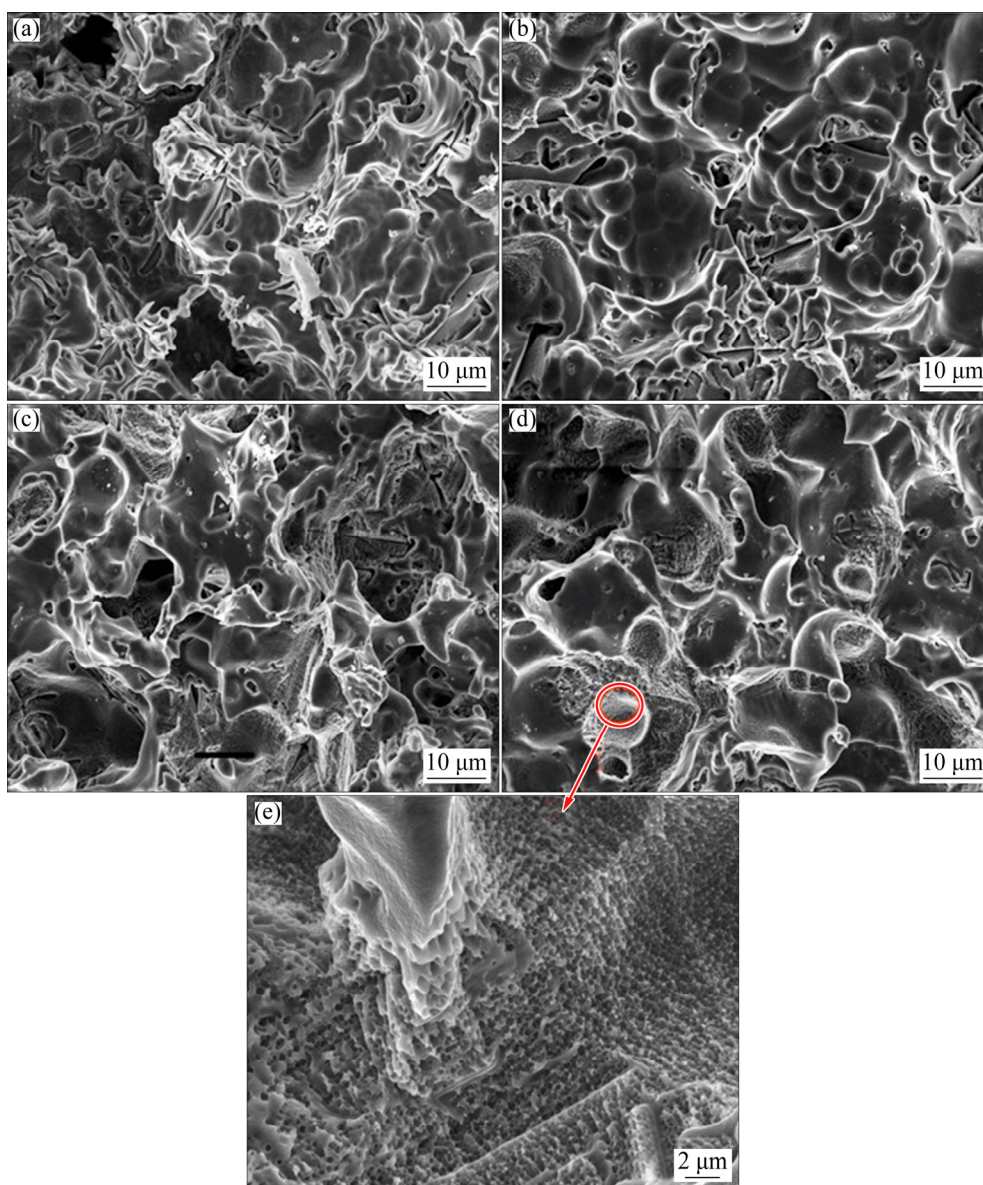

Fig. 4 SEM micrographs of corroded surfaces of AS21 (a), AS21−0.5Sn (b), AS21−1Sn (c) and AS21−2Sn (d, e) alloys after 72 h immersion in 3.5% NaCl

in 3.5% NaCl solution for 72 h. All the alloys exhibited corrosion pits on their surfaces, in which the deepest corrosion pits were observed on the surface of AS21 alloy. As the Sn content increased, most of the corrosion pits became relatively larger and shallower. The interior of a shallow corrosion pit in AS21−2Sn alloy is shown in Fig. 4(e). Evidently, the pits were covered by nanoscale holes. Due to their natural passivity, magnesium alloys undergo pitting corrosion under chloride ion exposure [23]. It has been reported that increasing Al content improved the overall corrosion resistance of Mg alloys by the formation of semi-protective Al-rich oxide layer and corrosion barrier effect of continuous β-Mg$_{17}$Al$_{12}$ phase network [24]. However, the formation of corrosion pits is generally progressed on heavy metal contamination and discontinuous β-Mg$_{17}$Al$_{12}$ phase, which has a higher potential relative to Mg matrix, especially when the Al content is low [18,20]. In as much as Mg$_2$Si phase has generally been accepted as one of the least potent cathodic intermetallics in magnesium alloys due to its same electrochemical potential with Mg (−1.65 V) [25] and the alloys in this study were considered to have similar amounts and distributions of heavy metal contamination and β-Mg$_{17}$Al$_{12}$ phase, the decrease in the formation of deep corrosion pits was believed to be primarily due to the change in the chemical composition of second phases and α-Mg matrix. Influence of the compositional change in α-Mg matrix on the corrosion resistance has been reported in several studies [26,27]. SONG et al [26] reported that the corrosion resistance of α-Mg matrix in AZ91D alloy increased as its Al content increased. In addition, the grain interiors of AZ91 alloy were found to be pitting corrosion initiation sites and they exhibited higher corrosion rate than the regions near grain boundaries. As outlined above, the gray network structure was enriched in Sn and Al due to segregation during solidification, indicating that the large and shallow pits in Sn-containing alloys, which led to a higher corrosion resistance, were due to the solute element enrichment that could enhance the formation of protective film [28]. Accordingly, the formation of nanoscale holes inside the shallow pits was thought to be due to the compositional inhomogeneity of α-Mg matrix.

In order to get a better insight on the effect of Sn addition on the initiation and propagation of the corrosion of AS21 alloy, microstructure investigations after immersion in 3.5% NaCl solution for 72 h were conducted and presented in Fig. 5. It is clear that the surface of AS21 alloy had more corrosion attacks than AS21−2Sn alloy. The partial protective film on the surface of the alloys was either broken by secondary phases or α-Mg grain interiors. The corrosion propagated preferentially on these cathodic sites through the inner

parts of the surface which led to the formation of deep corrosion pits after 72 h immersion as indicated by red arrows in Fig. 5. The corrosion pits on AS21 alloy were much larger and deeper than those on AS21−2Sn alloy. It is also evident that some undermining of Mg$_2$Si particles occurred due to the severe dissolution of α-Mg. On the other hand, severe corrosion propagations in AS21−2Sn alloy were prevented on α-Mg matrix.
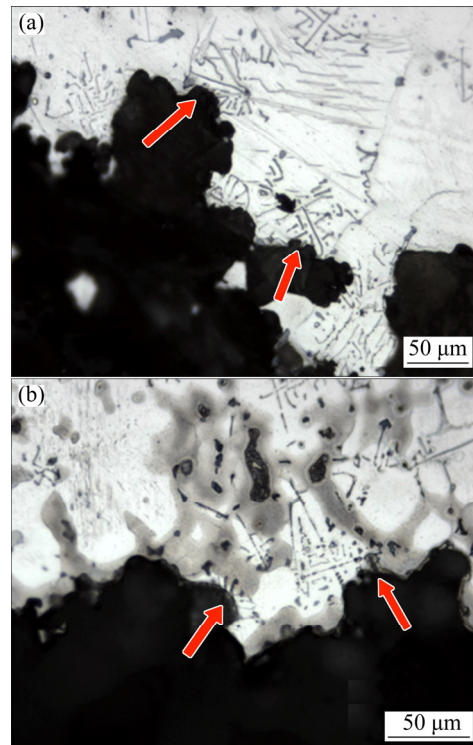

Fig. 5 Optical micrographs of cross sections of AS21 (a) and AS21−2Sn (b) alloys after immersion in 3.5% NaCl for 72 h

Figure 6 shows potentiodynamic polarization curves of the alloys with an inset graph showing the change in corrosion current densities (J_{corr}) derived from the curves as a function of Sn content. The calculated corrosion rates according to Eq. (2) are also given in Table 3. The cathodic and anodic reactions during electrochemical corrosion testing are generally expressed as follows: the cathodic branch governs the hydrogen evolution whereas the anodic branch describes the dissolution of Mg [29]. As seen in Fig. 6, the cathodic polarization branches of the alloys exhibited larger changes than the anodic polarization branches. At the same potential, a gradual decrease in the cathodic current density was observed with increasing Sn content whereas the anodic current density showed an increase after Sn addition in AS21 alloys. That is to say, Sn addition resulted in an effective suppression of cathodic corrosion reactions while it promoted the anodic corrosion reaction. As shown in Table 3, the corrosion current densities sharply decreased with 0.5 wt.% Sn addition and it showed a gradual
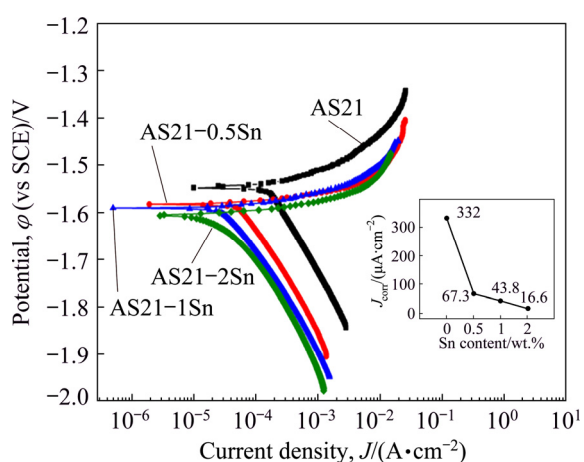
Fig. 6 Potentiodynamic polarization curves of AS21−*x*Sn alloys with inset graph showing J_{corr} values obtained from curves as function of Sn content

decrease up to 2 wt.% Sn addition. Since the decrease in corrosion current densities by Sn addition was governed by cathodic reactions, corrosion improvement on AS21 alloy by Sn addition can be expressed by hydrogen evolution mechanism. It was reported that Sn addition to Mg and its alloys can reduce the discharge of hydrogen ions at the surface because Sn is known for a high hydrogen overvoltage [16,30,31]. It was also suggested that the $Mg(OH)_2$ layer on the surface can be stabilized by Sn alloying and accordingly decreased the corrosion rate [30]. It should be noted that the corrosion potentials (φ_{corr}) decreased to less noble values as the Sn content increased. This is also because the cathodic reactions and hydrogen evolution rate were lowered by Sn addition, resulting in lower φ_{corr} values. Similar trends in the change of J_{corr} and φ_{corr} values as a function of Sn content in Mg alloys have been reported elsewhere [30,32]. Moreover, as Table 3 provides a direct comparison between the corrosion rates calculated from mass loss measurements and Tafel extrapolations, one can notice that the corrosion rates calculated from mass loss measurements were much higher than those calculated from Tafel extrapolations. This is because the proper application of Tafel extrapolation is violated by hydrogen evolution in the anodic region on the film-free areas for magnesium alloys and thus, it may not give correct

estimations of corrosion rates [33,34]. Therefore, care must be taken in analysing corrosion rates from Tafel extrapolation methods. On the other hand, it can be seen in Table 3 that the corrosion rates derived from immersion and Tafel extrapolation methods showed the same trend as a continual decrease in the corrosion rate of AS21 alloy with increasing Sn content.

The Nyquist plots of AS21−*x*Sn alloys with corresponding equivalent circuit are represented in Fig. 7. The EIS spectra of the alloys showed similar characteristics by exhibiting two capacitive loops at high and low frequencies. No inductive loop was observed in the studied alloys. The difference in the diameter of the arcs indicates that the corrosion rate of each alloy is different depending on the microstructural changes by Sn alloying. Generally speaking, the high frequency capacitive loop characterizes the relaxation process of electrochemical reaction which corresponds to corrosion of sample [35]. The low frequency capacitive loop is associated with the presence of protective surface film affecting the corrosion process [36]. In Fig. 7, as the Sn content increased, the diameter of the high frequency capacitive loop increased, implying that the Sn addition continually improved the corrosion resistance of AS21 alloy. Additionally, low frequency capacitive loops are also larger in the Sn-containing alloys compared to AS21 alloy, indicating more stable protective film on the surface. The EIS results are also fitted according to the equivalent circuit shown as the inset image in Fig. 7 and the fitting data are presented in Table 4. In this model, R_s, R_t and R_f denote solution resistance, charge transfer resistance and corrosion product (film) resistance. CPE_1 (constant phase element) is the capacity of the film and CPE_2 is the electric double layer capacity between the sample and solution. In general, materials having better corrosion resistance exhibit higher R_t and R_f values due to the difficulty of transfer charges between solution and the sample [37]. As seen in Table 4, with increasing Sn content, R_t and R_f values increased, indicating that Sn addition improved the corrosion resistance of AS21 alloy.

The corroded surfaces after 6 h immersion without the removal of corrosion products are illustrated in Fig. 8. It is evident that AS21 alloy exhibited poorer corrosion

Table 3 Corrosion rate of alloys obtained from immersion and potentiodynamic polarization tests

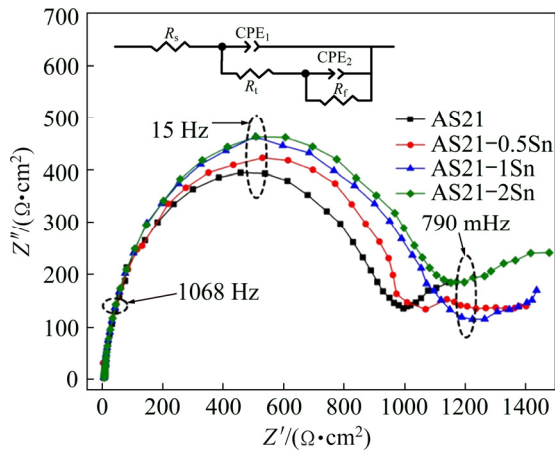| Alloy	Immersion		Polarization		
	$\Delta W/$ (mg·cm^{-2}·d^{-1})	$P_w/$ (mm·a^{-1})	$\varphi_{corr}/$V	$J_{corr}/$ (μA·cm^{-2})	$P_i/$ (mm·a^{-1})
AS21	18	37.35	−1.550	332	7.50
AS21−0.5Sn	15.4	31.41	−1.590	67.3	1.50
AS21−1Sn	9.6	19.36	−1.580	43.8	0.96
AS21−2Sn	6.7	13.11	−1.610	16.6	0.35

Fig. 7 Nyquist plots with inset graph showing equivalent circuit of EIS spectra of AS21−xSn alloys

Table 4 Fitting results of EIS data for AS21−xSn alloys

Alloy	R_s/ $(\Omega \cdot cm^2)$	R_t/ $(\Omega \cdot cm^2)$	R_f/ $(\Omega \cdot cm^2)$	CPE_1/ $(\mu F \cdot cm^2)$	CPE_2/ $(\mu F \cdot cm^2)$
AS21	4.8	326.3	895.3	980	19.8
AS21−0.5Sn	6.2	436.6	936	890	13.4
AS21−1Sn	5.5	476.2	1021	910	14.5
AS21−2Sn	6.4	610.4	1071	766	15.6

surface after 6 h immersion compared with Sn-containing alloys, in which the corrosion product formation in AS21 alloy seemed to be larger and more localized. Increasing Sn addition up to 1 wt.% resulted in a more uniform and finer oxide formation. Besides, AS21−2Sn alloy showed a mixture of fine oxide formation and uncorroded regions due to locally
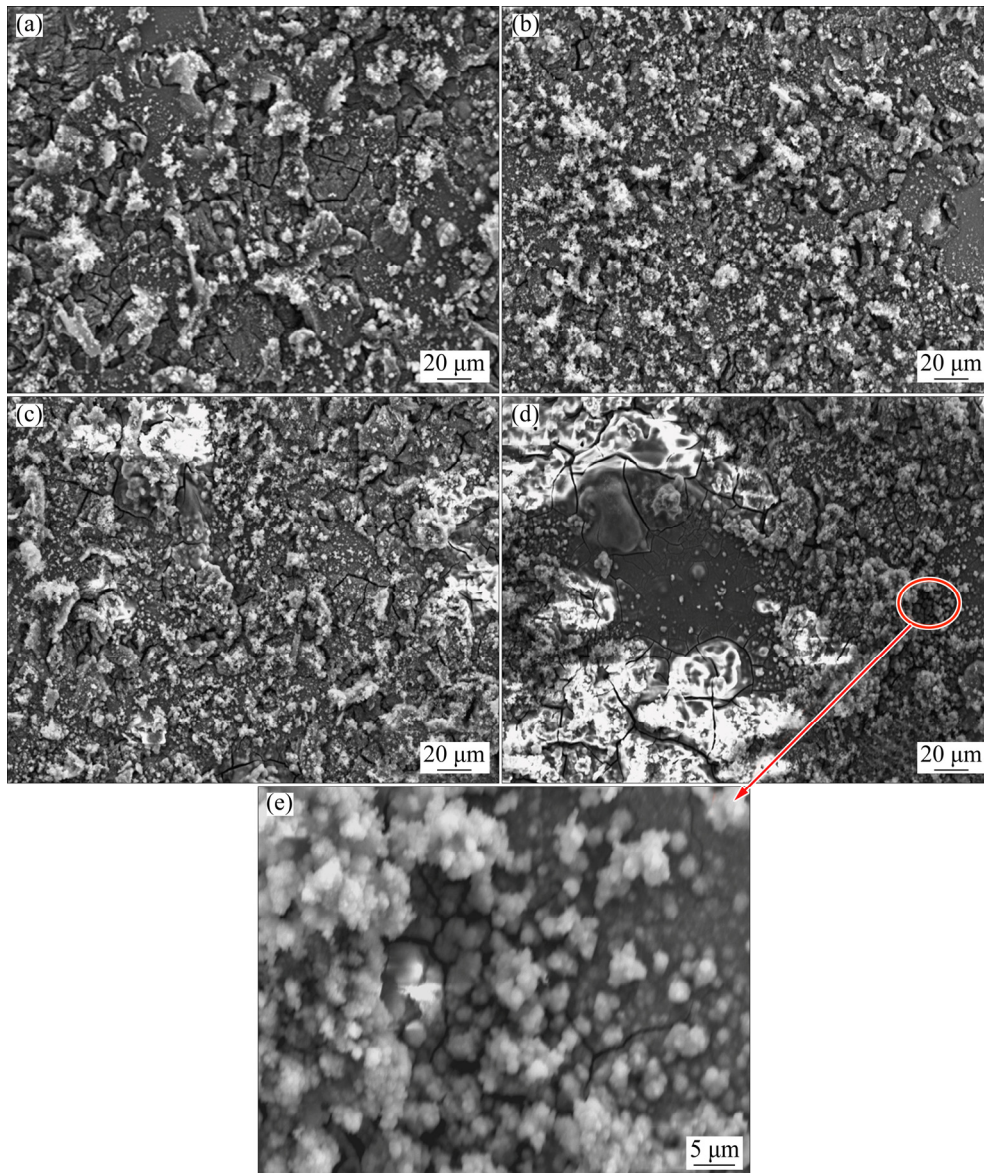

Fig. 8 SEM micrographs of corroded surfaces after 6 h immersion in 3.5% NaCl without removal of corrosion products: (a) AS21; (b) AS21−0.5Sn; (c) AS21−1Sn; (d, e) AS21−2Sn
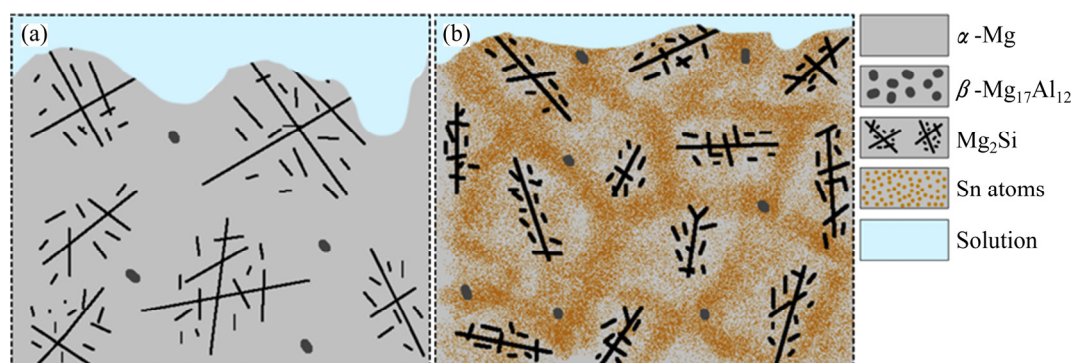
Fig. 9 Schematic image of corrosion development in AS21 (a) and AS21−2Sn (b) alloys

stabilized protective oxide layer caused by Sn segregation during solidification.

As outlined earlier, the corrosion was mainly initiated near the secondary phases or α-Mg interiors in the vicinity of second phases. Because the size and distribution of β-Mg$_{17}$Al$_{12}$ phase were similar in all the alloys, the change in corrosion rate was not attributed to β-Mg$_{17}$Al$_{12}$ phase. It was reported that the corrosion rate of Mg−Al based alloys is accelerated by β-Mg$_{17}$Al$_{12}$ phase due to microgalvanic acceleration [24,38]. Therefore, one might expect that all second phases can lead to similar corrosion acceleration in Mg alloys. However, in the point of fact, different intermetallic particles can act as either corrosion accelerator or inhibitor depending on their size and distribution. For example, SRINIVASAN et al [39] showed that the corrosion resistance of AZ91 alloy was improved by Si and Sb additions due to fine and even distribution of polygonal Mg$_2$Si intermetallic rather than Chinese script type Mg$_2$Si. As shown in Fig. 2, coarse Chinese script type Mg$_2$Si in AS21 alloy was refined and transformed to Sn-containing Chinese script Mg$_2$Si phase (can also be denoted as Mg$_2$(Sn,Si)) after 2 wt.% Sn addition. It is thought that this fine distribution of Chinese script phase can also provide continuous protective film layer and retard the corrosion propagation. Furthermore, Sn elements in refined Chinese script Mg$_2$Si phase may contribute to suppression of corrosion initiation and propagation due to its high hydrogen overvoltage. As it is schematically illustrated in Fig. 9, the severe corrosion attacks that were observed on the surface of AS21 alloy were inhibited by the Sn-rich α-Mg regions and Sn-containing Mg$_2$(Sn,Si).

Based on the above analysis, the factors affecting the improvement on corrosion mechanisms of AS21 alloy by Sn addition can be explained in three aspects as follows: the first is the fine and even distribution of Chinese script type Mg$_2$Si phase that could contribute to production of protective film layer [39]. The second is the stabilization of the protective Mg(OH)$_2$ surface layer

by Sn addition and thus the corrosion rate was reduced [30]. The third is the formation of Sn-rich regions on α-Mg matrix and Sn-containing Chinese script type Mg$_2$Si phase, resulting in a retardation of hydrogen evolution due to the high hydrogen overvoltage of Sn. Thus, the increasing Sn content was the characteristic of the improved corrosion resistance of AS21 alloy.

4 Conclusions

(1) The microstructure of AS21 alloy consisted of α-Mg, divorced β-Mg$_{17}$Al$_{12}$ and coarse Chinese script type Mg$_2$Si intermetallic particles. As the Sn content increased, Chinese script type Mg$_2$Si phase contained Sn elements, forming a somewhat Mg$_2$(Sn,Si) phase. The size of Chinese script type Mg$_2$Si phase was refined and their distribution became more even and discrete after 2 wt.% Sn addition. Furthermore, a Sn-rich network structure formed throughout the microstructure with increasing Sn content.

(2) Corrosion resistance of AS21 alloy was gradually improved by increasing Sn additions. The improvement on the corrosion resistance was ascribed to fine and even distribution of Sn-containing Chinese script type Mg$_2$Si phase and Sn-rich regions, which suppressed the hydrogen evolution because of the higher hydrogen overvoltage of Sn and stabilization of the protective Mg(OH)$_2$ surface layer.

References

[1] POLMEAR I. Light alloys: From traditional alloys to nanocrystals [M]. 4th ed. Oxford; Burlington, MA: Butterworth−Heinemann, 2005.

[2] LUO A A. Magnesium casting technology for structural applications

[J]. Journal of Magnesium and Alloys, 2013, 1: 2−22.

[3]　LUO A, PEKGULERYUZ M O. Cast magnesium alloys for elevated temperature applications [J]. Journal of Materials Science, 1994, 29: 5259−5271.

[4]　BLUM W, ZHANG P, WATZINGER B, GROSSMANN B, HALDENWANGER H G. Comparative study of creep of the die-cast Mg-alloys AZ91, AS21, AS41, AM60 and AE42 [J]. Materials Science and Engineering A, 2001, 319−321: 735−740.

[5]　ZHANG P. Creep behavior of the die-cast Mg−Al alloy AS21 [J]. Scripta Materialia, 2005, 52: 277−282.

[6]　TANG S, ZHOU J, TIAN C, YANG Y. Morphology modification of Mg₂Si by Sr addition in Mg−4%Si alloy [J]. Transactions of Nonferrous Metals Society of China, 2011, 21: 1932−1936.

[7]　SENF J, BROSZEIT E, GUGAU M. Corrosion and galvanic corrosion of die casted magnesium alloys [C]//KAPLAN H I, HRYN J N, CLOW B B. Magnesium Technology 2000. John Wiley & Sons, Inc., 2000: 136−142.

[8]　EL SAWY E N, EL-SAYED H A, EL SHAYEB H A. Corrosion of Mg, AS31 and AZ91 alloys in nitrate solutions [J]. Journal of Alloys and Compounds, 2010, 492: 69−76.

[9]　CANDAN S, CANDAN E. A comparative study on corrosion of Mg−Al−Si alloys [J]. Transactions of Nonferrous Metals Society of China, 2017, 27: 1725−1734.

[10]　TUREN Y. Effect of Sn addition on microstructure, mechanical and casting properties of AZ91 alloy [J]. Materials & Design, 2013, 49: 1009−1015.

[11]　PARK S H, JUNG J G, YOON J, YOU B S. Influence of Sn addition on the microstructure and mechanical properties of extruded Mg−8Al−2Zn alloy [J]. Materials Science and Engineering A, 2015, 626: 128−135.

[12]　WANG F, DONG H, SUN S, WANG Z, MAO P, LIU Z. Microstructure, tensile properties, and corrosion behavior of die-cast Mg−7Al−1Ca−xSn alloys [J]. Journal of Materials Engineering and Performance, 2018, 27: 612−623.

[13]　KIM J K, OH S H, KIM K C, KIM W T, KIM D H. Effect of Sn addition on the precipitation behavior in AZ91 magnesium alloy [J]. Materials Transactions, 2017, 58: 963−966.

[14]　SEDIGHI O, SHABESTARI S G, YAVARI F. Investigation on the effect of Sn on solidification and microstructure of AZ91 magnesium alloy using cooling curve thermal analysis [J]. Thermochimica Acta, 2018, 667: 165−172.

[15]　PARK K C, KIM B H, JEON J J, PARK Y H, PARK I M. The influence of Sn addition on the corrosion behavior of Mg−5Al−1Zn alloy [J]. Materials Science Forum, 2009, 620−622: 153−156.

[16]　SONG G. Effect of tin modification on corrosion of AM70 magnesium alloy [J]. Corrosion Science, 2009, 51: 2063−2070.

[17]　ASTM G31−72. Standard practice for laboratory immersion corrosion testing of metals [S]. ASTM International, 2004.

[18]　ASTM G102−89. Standard practice for calculation of corrosion rates and related information from electrochemical measurements [S]. West Conshohocken, PA: ASTM International, 2015.

[19]　EVANGELISTA E, GARIBOLDI E, LOHNE O, SPIGARELLI S. High-temperature behaviour of as die-cast and heat treated Mg−Al−Si AS21X magnesium alloy [J]. Materials Science and Engineering A, 2004, 387−389: 41−45.

[20]　LUO A A, SACHDEV A K. Optimization of magnesium–aluminum–manganese alloys and the effects of tin and rare earth additions [C]//Magnesium Technology. TMS (The Minerals & Materials Society), 2009: 437−443.

[21]　HORT N, HUANG Y, KAINER K U. Intermetallics in magnesium alloys [J]. Advanced Engineering Materials, 2006, 8: 235−240.

[22]　KAINER K U. Magnesium: Proceedings of the 7th international conference on magnesium alloys and their applications [M]. John Wiley & Sons, 2007.

[23]　SONG G, ATRENS A. Corrosion mechanisms of magnesium alloys [J]. Advanced Engineering Materials, 1999, 1: 11−33.

[24]　PARDO A, MERINO M C, COY A E, ARRABAL R, VIEJO F, MATYKINA E. Corrosion behaviour of magnesium/aluminium alloys in 3.5wt.% NaCl [J]. Corrosion Science, 2008, 50: 823−834.

[25]　LUNDER O, NISANCIOGLU K, HANSEN R S. Corrosion of die cast magnesium-aluminum alloys [R]. Warrendale, PA: SAE Technical Paper, 1993: 930755.

[26]　SONG G, BOWLES A L, STJOHN D H. Corrosion resistance of aged die cast magnesium alloy AZ91D [J]. Materials Science and Engineering A, 2004, 366: 74−86.

[27]　SONG G, STJOHN D. Corrosion performance of magnesium alloys MEZ and AZ91 [J]. International Journal of Cast Metals Research, 2000, 12: 327−334.

[28]　NAM N D, THU V T H, THANH N T. Effect of tin on the corrosion of Mg−5Al based alloy in 3.5 wt.% NaCl Solution [J]. International Journal of Metallurgical & Materials Engineering, 2015, 1: 118.

[29]　CHANG J W, PENG L M, GUO X W ATRENS A, FU P H, DING W J, WANG X S. Comparison of the corrosion behaviour in 5% NaCl solution of Mg alloys NZ30K and AZ91D [J]. Journal of Applied Electrochemistry, 2008, 38: 207−214.

[30]　BOWLES A L, BLAWERT C, HORT N, KAINER K U. Microstructural investigations of the Mg−Sn and Mg−Sn−An alloy systems [C]//LUO A A. Magnesium Technology 2004. TMS (The Minerals, Metals & Materials Society), 2004: 307−310.

[31]　KUBÁSEK J, VOJTĚCH D, LIPOV J, RUML T. Structure, mechanical properties, corrosion behavior and cytotoxicity of biodegradable Mg−X (X=Sn, Ga, In) alloys [J]. Materials Science and Engineering C, 2013, 33: 2421−2432.

[32]　HA H Y, KANG J Y, KIM S G, KIM B, PARK S S, YIM C D, YOU B S. Influences of metallurgical factors on the corrosion behaviour of extruded binary Mg−Sn alloys [J]. Corrosion Science, 2014, 82: 369−379.

[33]　SONG G, ATRENS A. Understanding magnesium corrosion—A framework for improved alloy performance [J]. Advanced Engineering Materials, 2003, 5: 837−858.

[34]　ZHAO M C, LIU M, SONG G, ATRENS A. Influence of microstructure on corrosion of as-cast ZE41 [J]. Advanced Engineering Materials, 2008, 10: 104−111.

[35]　SONG G, ATRENS A, JOHN D S, WU X, NAIRN J. The anodic dissolution of magnesium in chloride and sulphate solutions [J]. Corrosion Science, 1997, 39: 1981−2004.

[36]　LIU M, SCHMUTZ P, UGGOWITZER P J, SONG G, ATRENS A. The influence of yttrium (Y) on the corrosion of Mg−Y binary alloys [J]. Corrosion Science, 2010, 52: 3687−3701.

[37]　TONG L B, ZHANG Q X, JIANG Z H, ZHANG J B, MENG J, CHENG L R, ZHANG H J. Microstructures, mechanical properties and corrosion resistances of extruded Mg−Zn−Ca−xCe/La alloys [J]. Journal of the Mechanical Behavior of Biomedical Materials, 2016, 62: 57−70.

[38]　SONG G, ATRENS A, DARGUSCH M. Influence of microstructure on the corrosion of diecast AZ91D [J]. Corrosion Science, 1998, 41: 249−273.

[39]　SRINIVASAN A, NINGSHEN S, KAMACHI MUDALI U, PILLAI U T S, PAI B C. Influence of Si and Sb additions on the corrosion behavior of AZ91 magnesium alloy [J]. Intermetallics, 2007, 15: 1511−1517.

添加锡对 AS21 镁合金显微组织和耐腐蚀性能的影响

Huseyin ZENGIN[1], Yunus TUREN[1], Hayrettin AHLATCI[1],

Yavuz SUN[1], Abdullah Cahit KARAOĞLANLI[2]

1. Department of Metallurgical and Materials Engineering, Karabuk University, Turkey;

2. Department of Metallurgical and Materials Engineering, Bartın University, Turkey

摘　要：研究添加锡对 AS21 镁合金显微组织和耐腐蚀性能的影响。采用低压压铸法制备分别添加 0、0.5、1 和 2 wt.% Sn 的 AS21 合金。用光学显微镜和扫描电镜进行显微组织表征，通过在 3.5% NaCl 溶液中浸渍和电化学腐蚀试验研究合金的耐腐蚀性能。微观检测结果显示，AS21 合金中含有 α-Mg、孤立的 β-$Mg_{17}Al_{12}$ 和汉字状 Mg_2Si 金属间化合物相。随着 Sn 含量的增加，Mg_2Si 相的分布变得更加离散和致密。当 Sn 添加量为 2 wt.%时，形成遍布于整个组织的富 Sn 网状结构，汉字状组织由短棒状的 Mg_2Si 相排列组成。持续浸泡腐蚀试验表明，随着锡含量的增加，AS21 合金的降解程度不断降低，当锡含量为 2 wt.% 时，AS21 合金的腐蚀速率降低约 65%。电化学腐蚀试验也表明，随着锡含量的增加，AS21 合金的耐蚀性逐渐提高。

关键词：AS21；镁合金；锡添加；显微组织；腐蚀

(Edited by Bing YANG)